Mesoscale Simulation of Supercritical, Subcritical, and Transcritical Flow along Coastal Topography

STEPHEN D. BURK AND TRACY HAACK

Marine Meteorology Division, Naval Research Laboratory, Monterey, California

R. M. SAMELSON

College of Oceanic and Atmospheric Sciences, Oregon State University, Corvallis, Oregon

(Manuscript received 10 April 1998, in final form 29 November 1998)

ABSTRACT

A mesoscale atmospheric model is used to address the characteristics of stratified flow bounded by a side wall along a varying coastline. Initial Froude number values are varied through alteration of marine inversion strength, permitting examination of supercritical, subcritical, and transcritical flow regimes encountering several coastal configurations. Consistent with shallow water models, sharp drops in boundary layer depth and flow acceleration occur in flow rounding convex bends; however, significant flow response occurs in the stratified layer aloft, which is unexplained by conventional shallow water theory. The strongest flow acceleration occurs in the transcritical case while, regardless of inversion strength, the deformation of the isentropes aloft shows general structural similarity.

Advection of horizontal momentum is an important component of the horizontal force balance. A simulation having several coastline bends exhibits a detached, oblique hydraulic jump upwind of a concave bend that strongly blocks the flow. For the single-bend case, a shallow water similarity theory for stratified flow provides qualitative, and partial quantitative, agreement with the mesoscale model, in the boundary layer and aloft. Horizontal structure functions for these similarity solutions satisfy a set of equivalent shallow water equations. This comparison provides a new perspective on previous shallow water models of supercritical flow around coastal bends and suggests that the existence of the supercritical flow response may depend more on the presence of a low-level jet than on a sharp boundary layer inversion.

1. Introduction

Coastal orography can have important effects upon a shallow, inversion-capped mesoscale wind field. Along the northern California coast, strong, northerly surface winds and a stable inversion are particularly pronounced during the summer. Winant et al. (1988) identify several typical summertime flow patterns in the region between Point Arena and Point Reyes, one of which displays strong winds with marked along-coast variability over short fetches. Studies in other geographical coastal areas have noted similar flow behavior (Freeman 1950; Enfield 1981; Elliott and O'Brien 1977). The orographically forced wind stress curl can impact ocean upwelling (Enriquez and Friehe 1995). More recently trapped waves and orographically controlled flows have been the focus of the Coastal Observation and Simulation with Topography (COAST) and Coastal Waves 1996 (CW96) experiments along the U.S. west coast (Rogers et al. 1998).

Winant et al. (1988) note that within the regime having strong coastal wind variability, characteristics of a supercritical channel flow appear that include oblique expansion waves and hydraulic jump features. Supercritical flow is analogous to supersonic flow in that expansion fans and shock features are manifest in both. Whereas supersonic conditions occur when the flow relative to an object exceeds the speed of sound, supercritical conditions occur when the wind speed exceeds the phase speed of internal gravity waves. Supercritical flow behavior, with expansion waves and internal jumps, was observed in CW96 as well. A downward-looking lidar in a research aircraft permitted boundary layer depth changes to be related to the measured flow dynamics. In order to further understand the essential dynamics of such flows, Samelson (1992) presents a series of idealized, single-layer fluid simulations along a varying, wall-bounded coastline. He finds that marine atmospheric boundary layer (MABL) friction dramatically alters the form of an expansion fan in flow around

Corresponding author address: Stephen D. Burk, Marine Meteorology Division, Naval Research Laboratory, 7 Grace Hopper Avenue, Monterey, CA 93943-5502.
E-mail: burk@nrlmry.navy.mil

a bend, and that stress variations of 10%–50% occur in such orographically forced supercritical flows. Burk and Thompson (1996), using a continuously stratified mesoscale model, investigated the dynamics of a low-level jet (LLJ) residing at the top of the MABL along the California coast. As part of that study, they examined LLJ enhancements in the lee of headlands such as Cape Mendocino and found that mountain wave processes could produce leeside accelerations of similar character and magnitude as those apparently due to supercritical flow behavior.

In this paper we seek to retain the realism possessed by a continuously stratified mesoscale model, while isolating supercritical, wall-bounded flow characteristics from those produced by mountain waves. To this end, we replace the realistic model topography of coastal California with very high, uniform terrain so as to separate the marine boundary layer from mountain waves aloft. The flow near the top of the terrain is specified to be very light so as to reduce mountain wave effects. Further, we use simple, piecewise linear coastlines. This permits solution to the wall-bounded flow problem in a manner similar to shallow water approaches, while still resolving detailed vertical structure and addressing the role of continuous stratification. The impact of varying the upstream Froude number (the ratio of the flow speed to the phase speed of internal waves) upon flow around and downstream of a coastal bend will be examined. We address not only flows that are fully supercritical on each side of a bend, but we examine subcritical flows and flows that are transcritical, that is, contain regions of both subcritical and supercritical flow.

Section 2 presents a model description and describes the nature of the simulations. In section 3 we present results for flows of different Froude number around a single, convex bend, while section 4 contains an examination of the momentum budget of the flow in section 3. Section 5 describes the response to the addition of a concave bend south of the first bend, followed by another convex bend. The concave bend is found to aid in the creation of a hydraulic jump–like feature, while expansion fans form about each of the convex bends. Section 6 contains discussion of shallow water similarity solutions and the trapping of vertically propagating gravity wave modes. Section 7 has concluding remarks.

2. Setup of mesoscale simulations

a. Model description

Hodur (1997) describes the Naval Research Laboratory's (NRL) Coupled Ocean/Atmosphere Mesoscale Prediction System (COAMPS) in a recent article. Use here is made only of the atmospheric portion of COAMPS. Although COAMPS contains an extensive suite of physical parameterizations, for our purpose we run the model using many simplifications. In particular, the model atmosphere is taken to be dry and radiation is neglected. COAMPS is a semi-implicit, compressible, nonhydrostatic model that uses a terrain-following sigma coordinate system. Generally it is run as an NWP model and uses an extensive data assimilation procedure to define its initial state, but that is unnecessary for our idealized simulations. In 1998 COAMPS became the U.S. Navy's operational mesoscale model and now provides forecasts for several separate regions around the globe. COAMPS has been validated and its results documented recently in various studies (e.g., Doyle 1997; Thompson et al. 1997; Rogers et al. 1998; Hodur 1997).

While COAMPS can be run with multiple grid nests, a single mesh having a 9-km horizontal grid increment in both horizontal directions is used in these simulations. The grid has 88 points in the x direction (east–west), 108 points in y (north–south), and 30 levels in the vertical. The vertical spacing is highly nonuniform, with half of the vertical levels being placed in the first kilometer so as to adequately resolve the boundary layer. The first grid point above the surface is at 10 m and the grid top is at 26.1 km. The average vertical spacing in the lowest 400 m where the MABL resides is $\sim$40 m.

b. Initial and boundary conditions

The initial set of simulations involves northerly flow around a single, linear bend in the coastline. North of the bend the coast is oriented north–south, with ocean to the west of the coastline. A convex bend is formed, at a latitude of 40°N, by a coastline that moves one grid point east for every two moved south, as shown in Fig. 1. This ensures that the coastline falls on the grid points and results in $\varphi \cong 26.6°$ (Fig. 1), which is similar to the value (30°) used by Samelson (1992). To simulate the ''wall,'' the terrain height rises abruptly from sea level to 2 km over four grid intervals and remains at a constant 2 km farther inland from the coast.

The atmosphere is specified to be horizontally homogeneous initially, with a 400-m-deep well-mixed boundary layer over the ocean that is capped by an inversion, and then a uniformly stable potential temperature increase above. The surface temperature is fixed at the initial near-surface air temperature, both over water and land. Thus, the surface heat fluxes are zero initially but can become nonzero during the simulation if the near-surface air temperature changes. As a test, however, we ran the benchmark case with zero surface heat flux throughout the simulation and found that it altered the results only slightly. In all but one simulation the actual and geostrophic wind are initially specified to be northerly with a magnitude of 15 m s^{-1} in the marine layer, decreasing to a small value near the top of the terrain. This decrease in wind speed above a maximum at the MABL top is a typical feature of northerly flow along the California coast during the summer (Winant et al. 1988; Bridger et al. 1993; Rogers et al. 1998). The surface roughness length over land is specified as 1 cm, while over water it is computed based on

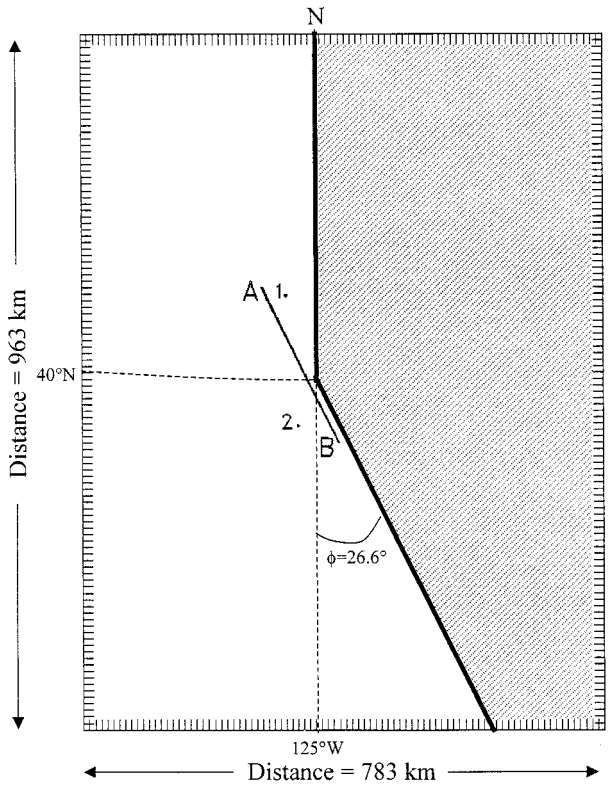

FIG. 1. Full model domain with coastal bend used for mesoscale model simulations. Cross-section plane, A–B, and points 1 and 2 are used for many subsequent figures; land (shaded) and ocean (blank).

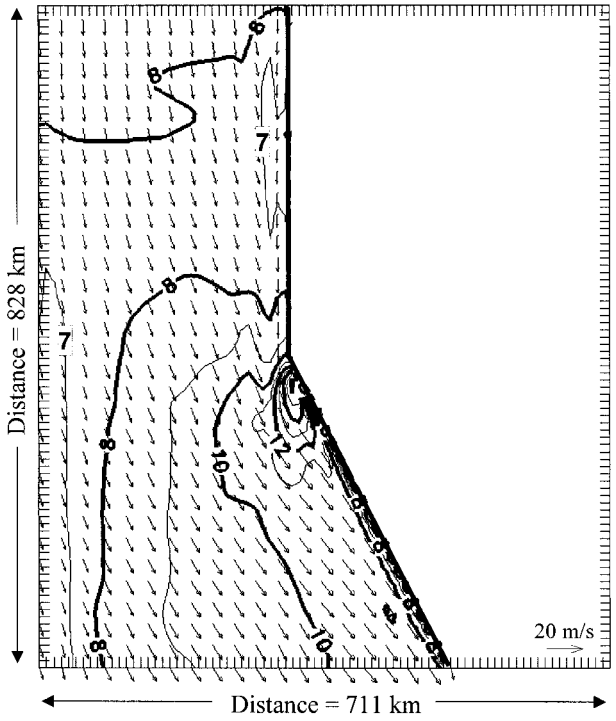

FIG. 2. 10-m wind vectors and isotachs (m s^{-1}) at hour 6 of the benchmark simulation.

Charnock's expression. Fixed inflow/outflow conditions are used at the lateral boundaries and integration proceeds until the flow in the interior of the domain attains near stationarity, thereby avoiding transient solutions. Previous shallow water approaches that we will compare with have often assumed stationarity as their starting point. The fixed boundary conditions create some artificial gradients, particularly at the southern boundary, as the flow in the interior develops. These artificial gradients, however, are confined to the vicinity of the boundary and there is no evidence that they affect the flow in the interior of the domain.

As a benchmark case, we select MABL parameters such that the initial Froude number based on the boundary layer thickness and inversion strength upwind of the bend is near 1.0, which represents the transition point from subcritical to supercritical flow. With a geostrophic wind of 15 m s^{-1}, the integrated actual wind in the MABL attains a stationary value near 12 m s^{-1}. With a MABL depth, h, equal to 400 m, and a jump in potential temperature, $\Delta\Theta$, equal to 10°C at the MABL top, the Froude number

$$\mathrm{Fr} = U(g'h)^{-1/2}$$

is Fr $\cong$ 1.0. Here g' is the reduced gravity, given by $g(\Delta\Theta/\Theta)$. We conduct several simulations in which the Froude number of the upstream flow is varied by altering the inversion strength to 5° and 20°C [Bridger et al. (1993); present aircraft observations along the California coast showing inversions of ~20°C]. One simulation is conducted in which the actual and geostrophic wind are initially set at 2 m s^{-1} in the MABL and decrease to near zero at 2 km. This provides a simulation in which the flow remains fully subcritical on either side of the bend. This simulation uses $\Delta\Theta$ = 10°C as in the benchmark.

3. Simulations having a single coastal bend

a. Benchmark case

In this simulation, flow upstream of the bend is transitional between subcritical and supercritical. Based on shallow water model solutions for supercritical flow (e.g., Samelson 1992) we anticipate acceleration within the MABL as the flow rounds the bend. The MABL depth is expected to decrease, the Froude number to increase, and the flow field to show characteristics of an expansion fan.

Figure 2 shows the near-surface (10 m) wind field after 6 h when the flow has approached stationarity. The display in Fig. 2 represents a subset of the entire model domain. Upstream of the bend the flow is near 8 m s^{-1} and accelerates to a maximum of ~15 m s^{-1} as it rounds the corner. The resultant flow pattern looks very similar to the layer model solution that includes friction by Samelson (1992, his Fig. 4a). Figure 3a shows a vertical

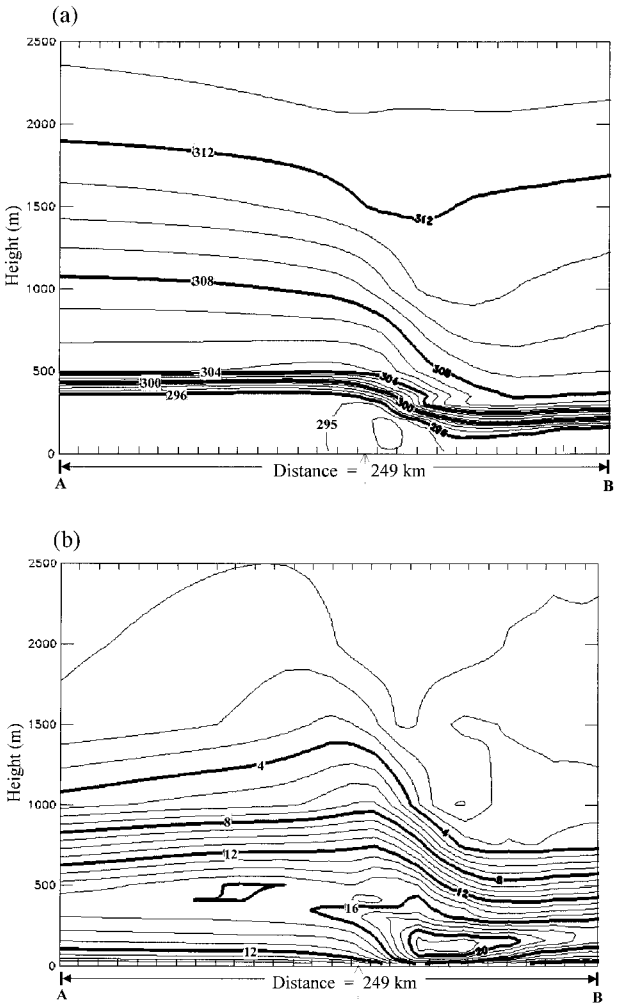

FIG. 3. (a) Potential temperature (K) at hour 6 of benchmark simulation along cross-section plane A–B of Fig. 1; and (b) wind speed (m s^{-1}). The arrow marks the location of the bend.

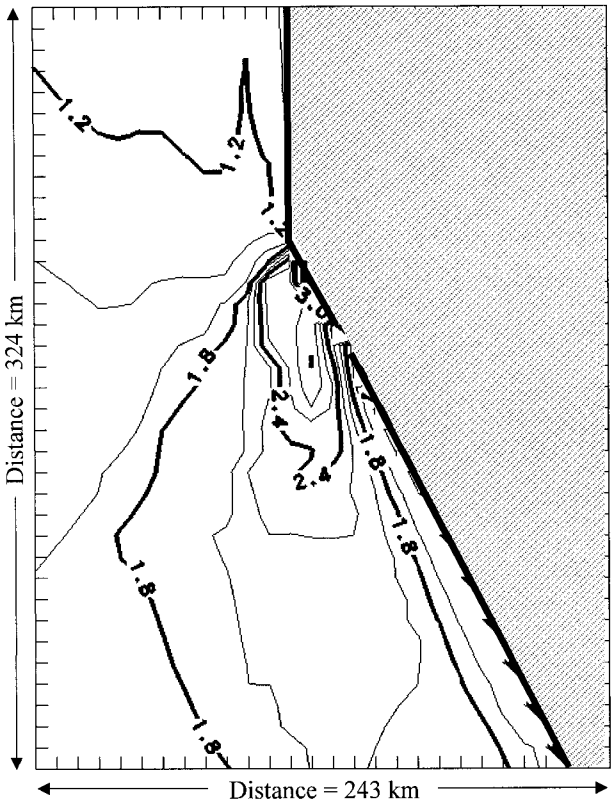

FIG. 4. Model-computed Froude number distribution at hour 6 of the benchmark simulation.

section of potential temperature (K) along line A–B indicated in Fig. 1. The MABL depth (as indicated by the inversion base) drops abruptly as the flow rounds the bend. The mixed layer collapses immediately south of the bend and then recovers to about half its upstream depth. Interestingly, the drop in height of the isentropes aloft is greater than that in MABL depth. For instance, the 308-K isentrope drops from ~1080 m at the left edge of Fig. 3a to a minimum of ~325 m, while the 296-K isentrope, which we take as roughly the MABL top, drops from ~400 to ~100 m. In addition to the potential temperature field, the COAMPS results also show considerable structural detail in the wind field (Fig. 3b). This vertical cross section of the wind field shows the flow accelerating to 21 m s^{-1} as it lowers, and a pronounced LLJ extends southward from the core of this wind maximum at the top of the MABL.

The near-surface acceleration as the MABL lowers and rounds the bend is clearly evident, while farther south of the bend the surface flow decelerates due, at least in part, to surface drag operating on a very shallow MABL. Perhaps a less anticipated feature is the development of a long wake of low-momentum air immediately above the MABL, which arises from low-speed air aloft being lowered. A cross section of vertical velocity along A–B (not shown) depicts strong, localized subsidence around the bend, which accounts for the substantial lowering of the isentropes and isotachs. Except immediately adjacent to the coast, the flow downstream of the bend remains supercritical as evidenced by a plot of Froude number (Fig. 4). A maximum of Fr ~3.0 is attained in the immediate lee of the bend.

The divergence field within the middle of the MABL (at 100 m) shows strong, positive divergence as the flow turns the bend, with convergence farther south where the flow encounters the coast (Fig. 5). This pattern, shown at hour 6 in Fig. 5, is persistent during the simulation. Since the initial state contains a uniform depth MABL, the strong, localized low-level divergence around the bend produces a substantial decrease in boundary layer depth there. This local change in fluid depth enhances the mesoscale pressure gradient. With time, the flow approaches a state of equilibrium where low-level divergence around the bend forces no further decrease in fluid depth. Rather, the tendency of the divergence to lower the MABL is offset primarily by hor-

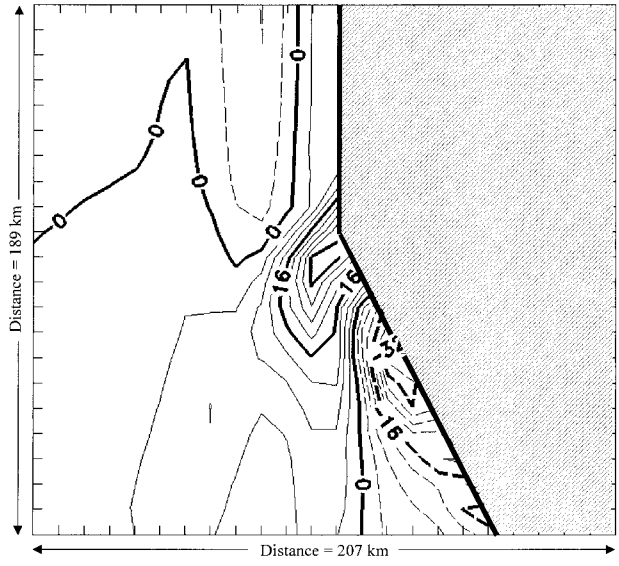

FIG. 5. Divergence (10^{-5} s^{-1}) at 100 m in the benchmark case at hour 6. (Dashed lines are negative, i.e., convergence). Only a portion of the full computational domain is shown.

izontal advection of deeper boundary layer depth from the flow upstream of the bend, as well as turbulent entrainment at the top of the MABL (momentum budgets that help quantify these relationships are presented in section 4).

b. Cases with altered inversion strength

We turn next to two cases in which slight alterations have been made from the benchmark case in order to change the criticality of the initial flow. In the first of these simulations (S1) the initial jump in potential temperature at the MABL top is set at 5°C, whereas it was 10°C in the benchmark. In the second simulation (S2) the initial inversion jump is set at 20°C. Otherwise the initial and boundary conditions of S1 and S2 are identical to those of the benchmark. Thus, we test the impact of altering the initial Froude number by varying the reduced gravity g', while keeping the initial wind speed, MABL depth, and pressure-gradient forcing unaltered.

1) FULLY SUPERCRITICAL SIMULATION, S1

With a 400-m-deep MABL, layer-average winds of 12 m s^{-1}, and $\Delta\Theta = 5$°C, the initial Froude number in this case is ~1.4. Figures 6a,b display vertical cross sections of potential temperature and wind speed at hour 6 along the same section as that in Figs. 3a,b. Comparison of Fig. 6a with Fig. 3a shows that the lowering of the boundary layer in S1 is not as pronounced as in the benchmark simulation despite the upstream flow being more supercritical in S1. Also, the isentropes aloft do not lower as much in S1 as in the benchmark even though the stratification above the inversion is identical in these two cases. In addition, the flow in S1 accelerates less than the benchmark. Figure 6b shows a maximum of 19 m s^{-1} in the flow rounding the bend, while the benchmark reached 21 m s^{-1} (Fig. 3b). These differences result from the alteration in the mesoscale pressure-gradient force (PGF). Although the slope of the MABL inversion in the vicinity of the bend is not greatly different in S1 than in the benchmark, the mesoscale pressure gradient in S1 is substantially weaker. This can be understood from consideration of the shallow water expression for the pressure-gradient force, PGF = $-(g\Delta\Theta/\Theta)\nabla h$, where the value of $\Delta\Theta$ in S1 is half that of the benchmark.

2) TRANSCRITICAL SIMULATION, S2

In S2 the inversion jump is 20°C initially, which yields an initial Froude number of ~0.8 (i.e., $2^{1/2}$ smaller than the benchmark). As the MABL lowers and the air accelerates upon rounding the bend, the flow becomes supercritical. Figure 7 shows the Froude number distribution for case S2 at hour 6 of the simulation. Samelson (1992) who dealt only with fully supercritical flow, for which the steady equations of motion are hyperbolic and can be solved by the method of characteristics, did not treat this type of transcritical flow.

Cross sections of potential temperature and wind speed, along the same section as used previously, are shown in Figs. 6c,d at hour 6. The drop in the isentropes shown in Fig. 6c is particularly abrupt in this instance. The inversion layer as demarcated again by the 288-K isentrope is less than 100 m deep as the MABL rounds the bend, while Fig. 6d shows that the boundary layer winds accelerate to a 25 m s^{-1} maximum. Downstream of this speed maximum, the wind slows and the MABL deepens. Also, the wind in S2 (Fig. 6d) shows substantially more acceleration in the upper portion of the MABL upstream of the bend than either in the benchmark simulation (Fig. 3b) or S1 (Fig. 6b), indicative that the stronger mesoscale PGF around the bend is impacting the subcritical flow farther upstream.

c. Low–wind speed simulation

SUBCRITICAL SIMULATION, S3

In order to include a case in which the flow remains subcritical throughout its passage around the coastal bend, we briefly discuss a simulation where the initial MABL wind speed is 2 m s^{-1}. For the very small surface stress values computed in this case, Charnock's expression gives molecular-scale values of roughness length, which correspond to unrealistically small values of the neutral drag coefficient. Thus, based on empirical drag coefficient expressions (e.g., Stull 1988, Table 7-3), we fix the neutral drag coefficient at 1×10^{-3}. Otherwise this simulation is identical to the benchmark.

As in previous simulations, a mesoscale PGF that

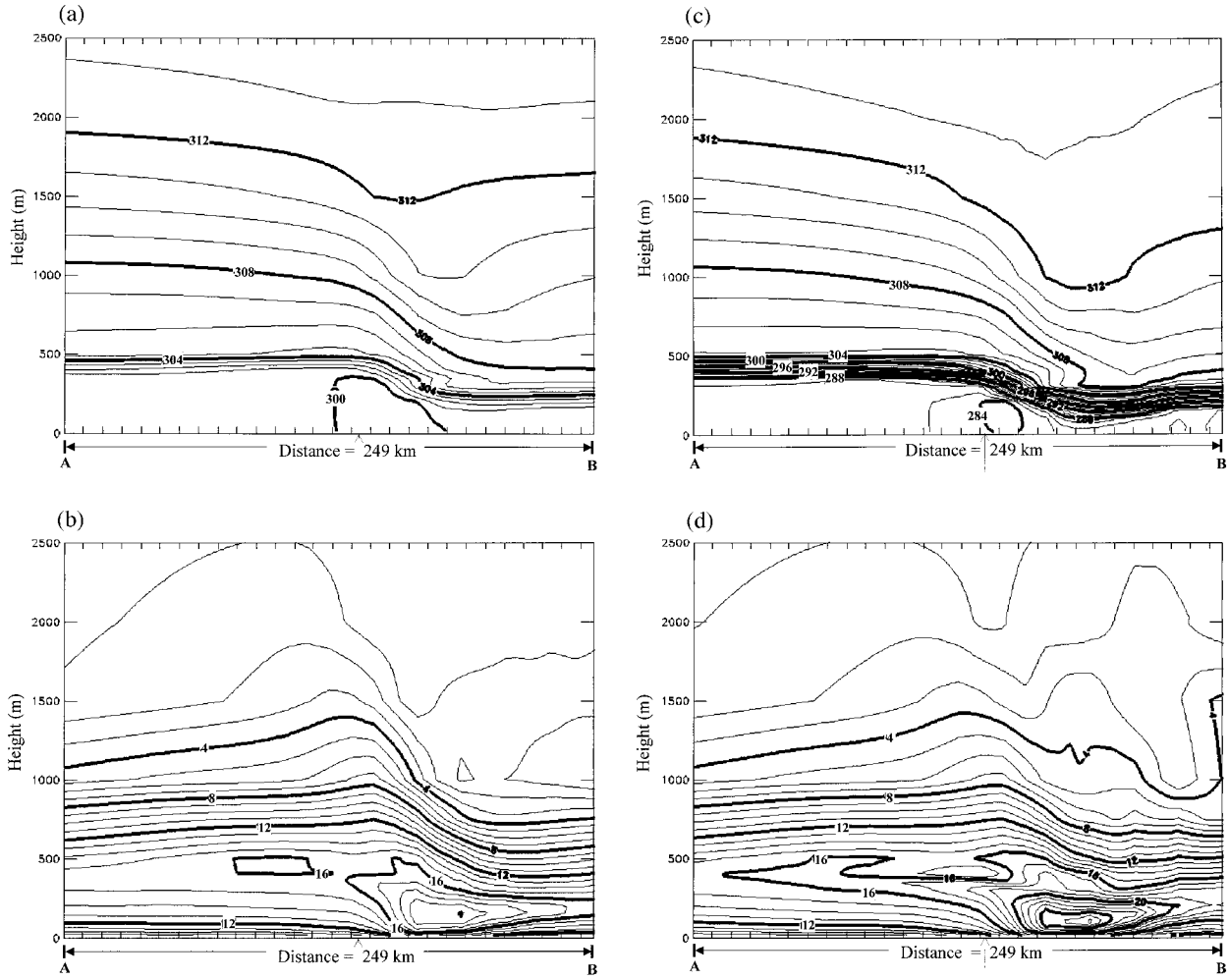

FIG. 6. (a) Potential temperature (K) in simulation S1 ($\Delta\Theta = 5°C$), (b) wind speed (m s^{-1}) in S1, (c) potential temperature (K) in S2 ($\Delta\Theta = 20°C$), and (d) wind speed (m s^{-1}) in S2; all at hour 6 for cross section A–B of Fig. 1. The arrow marks the location of the bend.

causes flow acceleration develops in the flow rounding the bend. However, the flow takes considerably longer to reach stationarity in this simulation than previous cases, with the weak advection terms building slowly to balance the forcing. By hour 24 the flow is approximately stationary and the Froude number well upstream of the bend is ~0.5. It increases to a maximum of ~0.7 near the corner. Most importantly, however, the resultant flow *pattern* differs sharply from the previous cases containing supercritical flow. Figure 8 shows the 10-m wind speed at hour 24 of the S3 simulation. The flow has a very broad region where it is stronger than its initial value of 2 m s^{-1}, and exhibits enhancement in speed near the coast well upstream of the bend. The speed maximum is actually attained slightly upstream of the bend.

Figures 9a,b display the potential temperature and wind speed at hour 24 in the same cross-section plane as used in previous simulations. There is no abrupt change in MABL depth evident in Fig. 9a, but rather only subtle variations in the inversion strength over a long fetch. The isentropes do indicate something of a trapped wave response in the first kilometer above the MABL top. The wind speed (Fig. 9b) shows a much more symmetrical pattern about the local maximum than was evidenced in the supercritical flow simulations. Thus, the mesoscale model indicates that very pronounced and recognizable differences are to be anticipated based upon the overall criticality of the flow.

4. Momentum budget analysis

It is of interest to examine the nature of the dynamic equilibrium attained by the flow in the simulations discussed thus far. In particular, we wish to see how equilibrium is achieved in the along- and cross-coast components of the momentum budget at a location upwind of the corner, as well as in the region of acceleration around the bend. The individual terms in the equations

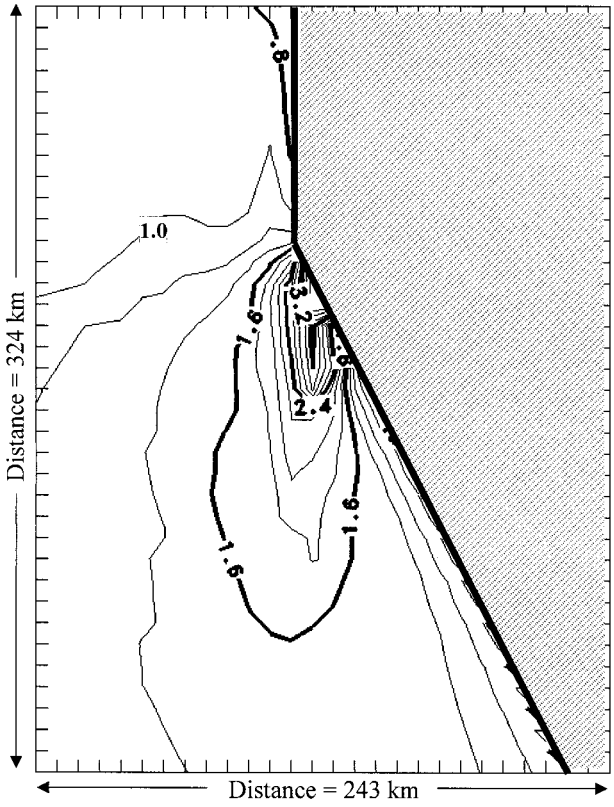

FIG. 7. Froude number distribution at hour 6 of simulation S2 ($\Delta\Theta$ = 20°C).

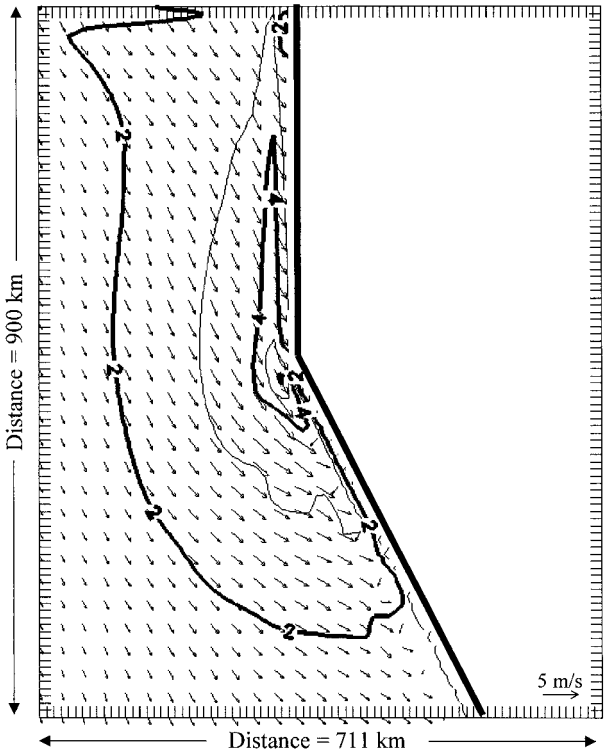

FIG. 8. 10-m wind speed at hour 24 of simulation S3 (light-wind case).

of motion are diagnosed directly from the COAMPS model, using the form

$$\underset{\text{(T)}}{\partial u/\partial t} = \underset{\text{(A)}}{-\mathbf{V}\cdot\nabla u} \underset{\text{(P)}}{-\rho^{-1}\partial P/\partial x} \underset{\text{(C)}}{+ fv} \underset{\text{(F)}}{+ F_x}, \quad (1)$$

$$\underset{\text{(T)}}{\partial v/\partial t} = \underset{\text{(A)}}{-\mathbf{V}\cdot\nabla v} \underset{\text{(P)}}{-\rho^{-1}\partial P/\partial y} \underset{\text{(C)}}{- fu} \underset{\text{(F)}}{+ F_y}, \quad (2)$$

where the x direction is taken to be the cross-coast component and y the along-coast component. (South of the bend the coordinate system is rotated such that the x direction is no longer east–west but rather is normal to the coast.) The labels used for identifying terms in the momentum budget are local tendency terms (T), advection (A), pressure-gradient force (P), Coriolis force (C), and stress divergence/''friction'' (F).

At point 1 of Fig. 1, located north of the bend, Fig. 10a shows the vertical distribution of terms in the cross-coast momentum budget, Eq. (1), at hour 6 of the benchmark case. Above the MABL, near geostrophy is obtained between the cross-coast pressure gradient and the Coriolis acceleration. Within the MABL the stress divergence offsets the PGF and is particularly significant near the surface, while the tendency and advection contributions remain small throughout. The vertical distribution of terms in the along-coast momentum budget, Eq. (2), at hour 6 (Fig. 10b) presents a more complex picture. First, however, it should be noted that at this location the along-coast pressure gradient is substantially weaker than the cross-coast value, so the abscissa in Fig. 10b necessarily differs from than that in Fig. 10a. Close to the surface in Fig. 10b the advection and Coriolis terms nearly cancel, leaving a near-antitriptic balance between stress divergence and pressure gradient. In the upper portion of the MABL, advection plays a significant role in balancing the pressure gradient force, while the local tendency shows the flow to be unsteady at the top of the MABL, perhaps indicative of a small inertial oscillation at that level. Although this northerly flow is not trapped by Coriolis turning, as a southerly flow would be along a north–south coastline (in the Northern Hemisphere); nevertheless, the presence of the wall boundary prevents geostrophic balance in the along-coast momentum component.

Figure 10c presents, for point 2 of Fig. 1 located south of the bend, the vertical distribution of terms in Eq. (1) at hour 6. The flow near point 2 has substantial spatial variability, however Fig. 10c shows that temporally it is very stationary. Advection and Coriolis force are the primary terms balancing the pressure gradient in this cross-coast component. The surface stress divergence is of importance only near to the surface. In the along-coast component (Fig. 10d), the stress divergence term plays a more prominent role in the lower half of the MABL. From that height up to about 1 km, as with the

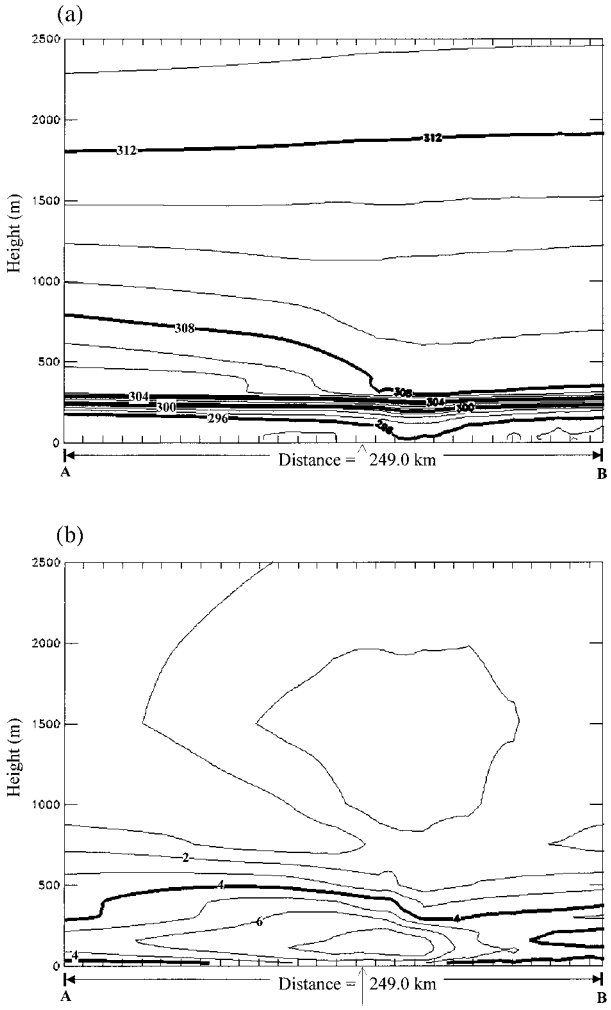

FIG. 9. (a) Potential temperature (K) and (b) wind speed (m s^{-1}) at hour 24 of simulation S3 in cross section A–B of Fig. 1. The arrow marks the location of the bend.

cross-coast component, advection and Coriolis acceleration are the primary terms balancing the pressure-gradient force. Above 1 km the flow is not quite stationary, but the wind there is very weak in any case.

Unlike point 1, the flow in the vicinity of point 2 is quite curved; the balance between advection, Coriolis acceleration, and pressure gradient in both momentum components suggests a gradient balance. If the curved flow near the top of the MABL is nearly in gradient balance around the bend, we should expect that

$$V_r^2/R + \text{PGF} + \text{Coriolis force} \cong 0, \qquad (3)$$

where V_r is the radial wind speed and R the radius of flow curvature. As a check, we solve Eq. (3) for V_r using average values from the model of Coriolis force and PGF within the MABL at point 2. This gives $V_r \cong 20$ m s^{-1}, which agrees well with the model MABL wind speed. Thus, we conclude that, near the bend, centripetal acceleration arising from flow curvature acts in concert with the Coriolis force to balance the mesoscale cross-stream PGF. The point-2 profiles indicate that in the along-stream momentum balance, friction and along-stream momentum advection are also important.

The momentum budgets for S1, our first sensitivity study, are qualitatively not greatly different than the benchmark. However, in S2 the MABL stress divergence (friction) is relatively stronger than the benchmark simulation. This results from the MABL winds being stronger and the boundary layer being shallower in S2. Thus, at point 2 within the MABL, S2 more nearly attains a balance between pressure gradient, centripetal acceleration, and friction.

The light-wind case (S3), which remains subcritical throughout, is near geostrophic balance in its cross-coast component both north and south of the bend. The along-coast momentum components are small, generally showing complex vertical structure for which no clear forcing dominates within the MABL.

Samelson and Lentz (1994) analyze the horizontal momentum budget in coastal flow using data from the Coastal Ocean Dynamics Experiment (CODE) as well as output from a single-layer model. However, they focus on a straight section of coast roughly 30 km downstream of the bend (Point Arena, in their case), rather than the immediate vicinity of the bend. Samelson and Lentz find the cross-coast balance is between advection, the Coriolis force, and the cross-coast PGF, while the along-coast balance is predominantly between vertical stress divergence and along-coast PGF. The COAMPS model produces a similar momentum balance (not shown) at a comparable location south of the bend in our simulations.

5. Simulation having three coastal bends

Before proceeding with the analysis of the single-bend flows, we consider a simulation that contains three coastal bends. The first bend is left unmodified, while the second and third bends are a consequence of the insertion of a 36 km (4 gridpoint) stretch of north–south-oriented coastline beginning about 80 km south of the first bend (Fig. 11). Each of the three bends turns by the same amount, 26.6°, with the first and third being convex and the second bend concave (this configuration is an idealized representation of the CODE coastline). Of particular interest here is the fact that the second bend is concave relative to the approaching flow; it extends into and blocks the accelerated flow around the first bend. Single-layer models have shown that oblique hydraulic jumps can occur under such circumstances (Samelson 1992; Rogerson 1999). Observations from CODE (Winant et al. 1988) also show strong indication of a hydraulic jump adjacent to a concave bend on the California coast. For an oblique compression jump to exist, the Froude number based upon the total wind speed does not necessarily transition through unity as the flow crosses the jump, but a Froude number com-

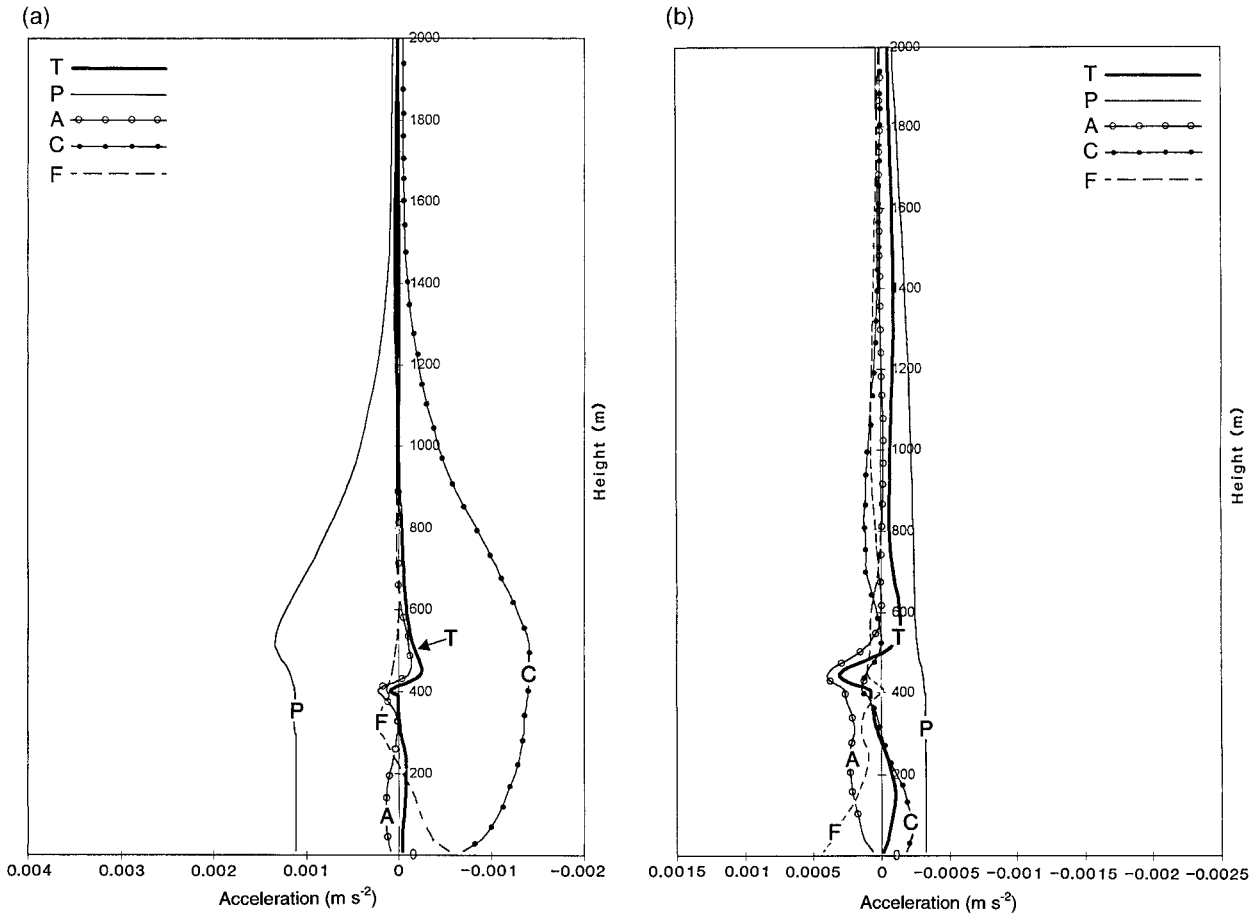

FIG. 10. (a) Vertical distribution of terms (m s^{-2}) in Eq. (1), the cross-coast momentum, at point 1 of Fig. 1; (b) those in Eq. (2), the along-coast momentum at point 1; (c) as in (a) except at point 2 of Fig. 1; and (d) as in (b) except at point 2 of Fig. 1.

puted using the wind speed *normal* to the jump does undergo such a transition. The boundary layer is expected to abruptly deepen, the surface pressure increase, and the wind speed normal to the jump decrease (creating a wind shift) as the flow transitions across such a shock front. Here we examine the extent to which such features are realized in the fully stratified mesoscale model.

Several simulations are conducted with three coastal bends using the same initial conditions as the benchmark case, as well as those of S1 and S2. The most pronounced hydraulic jump-like feature occurs using the S2 initial conditions ($\Delta\Theta = 20°C$) and here we present results only from that simulation. Figure 12a shows the 10-m wind vectors and isotachs at hour 4 (the jump is somewhat more pronounced at this time than hour 6). The flow at this level accelerates in an expansion fan around the first bend to a maximum of about 15 m s^{-1}. It then abruptly slows to less than 4 m s^{-1} with nearly calm wind along the coast. This area extends well north of the concave bend. Upon rounding the final convex bend, the flow again accelerates in an expansion fan and attains a maximum of about 13 m s^{-1}. Figure 12b zooms in on that portion of the flow in Fig. 12a having the most pronounced horizontal gradient. The striking features of this figure are the abruptness of the flow deceleration and the total reversal of wind direction at several grid points.

This pronounced gradient in wind speed is a strong indication of the presence of a hydraulic jump. This possibility may be further established by examining the distribution of Froude number at this time (Fig. 13). As previously noted, the S2 single-bend simulation is transcritical, with subcritical flow north of the first bend and supercritical south of the bend. In that single-bend simulation, the flow remains supercritical south of the bend. Figure 13 shows that blocking associated with the concave second bend causes the Froude number, even when computed using the total wind, to abruptly become subcritical along a line extending southwesterly away from the coast. This transition denotes the location of the hydraulic jump. It is detached from the vertex of the concave bend and intersects the coast at a point about halfway between the first and second bends. Ippen

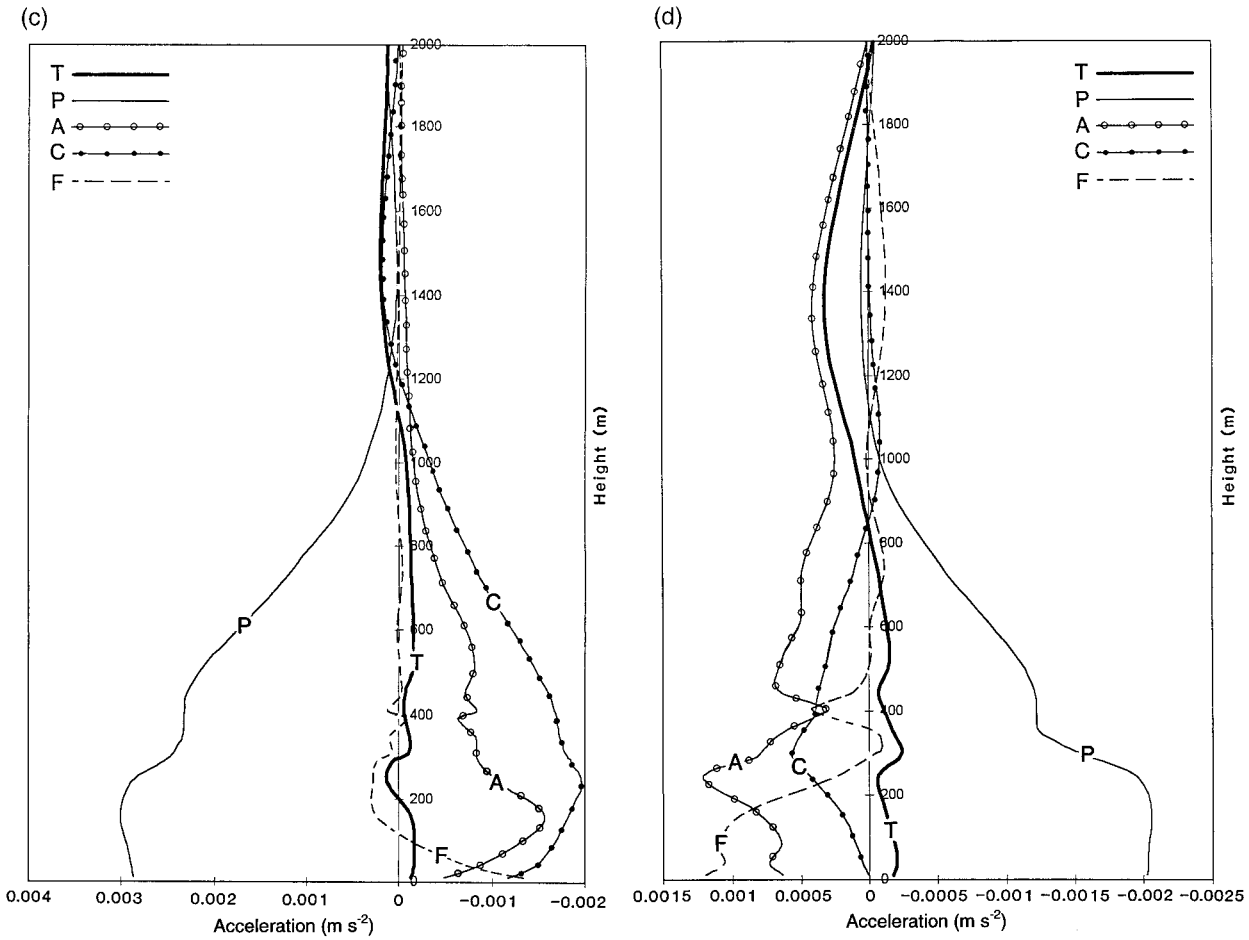

FIG. 10. (*Continued*)

(1951) presents shock–angle relationships for idealized, uniform supercritical flow along a sharp bend. His Fig. 8 indicates that an upwind Froude number ≥ 2.4 would be required to prevent a shock from detaching from a 26.6° concave bend, whereas our Fig. 13 shows substantially smaller upwind Fr values (even in the expansion fan following the first bend); and hence a detached shock is to be expected.

The presence of a jump also is demonstrated in the vertical cross sections of potential temperature (Fig. 14a) and wind speed (Fig. 14b) along section C–D of Fig. 11. Figure 14a shows the decrease in MABL depth in the expansion fan around the first bend, followed downstream by an abrupt increase in MABL depth. The jump even shows a head structure, resembling the leading edge of a bore, in which the isentropes bend back on themselves, indicative of an unstable lapse and convective overturning. A thin, neutrally stratified layer, overlying the MABL inversion, extends downwind from the head of the hydraulic jump. This thin, embedded neutral layer results from strong turbulent mixing driven by the convective overturning in the head of the hydraulic jump. Note also that the jump feature penetrates well into the stratified fluid above the MABL. The shapes of the isentropes aloft indicate that the hydraulic jump produces vertically propagating gravity wave modes that have very little tilt with height, very similar to those of a standing mountain wave (note, however, that the cross section does not intersect any terrain). The significance of such trapped modes is extensively explored in section 6.

Figure 14b shows the low-level wind maximum in the expansion fan, followed by a sharp decrease in wind speed across the oblique jump. While the gradient associated with the flow deceleration is most pronounced near the surface, there also is considerable deceleration in the thin, turbulent layer just above the MABL inversion. The surface pressure field (not shown) shows a drop of about 2 hPa in the flow rounding the first bend. However, the pressure abruptly rises by about this amount upon crossing the oblique jump. South of the jump, there is an extensive region where the pressure field is very flat. Another, weaker pressure drop occurs in association with the expansion fan around the second convex bend. There is no further blocking south of this

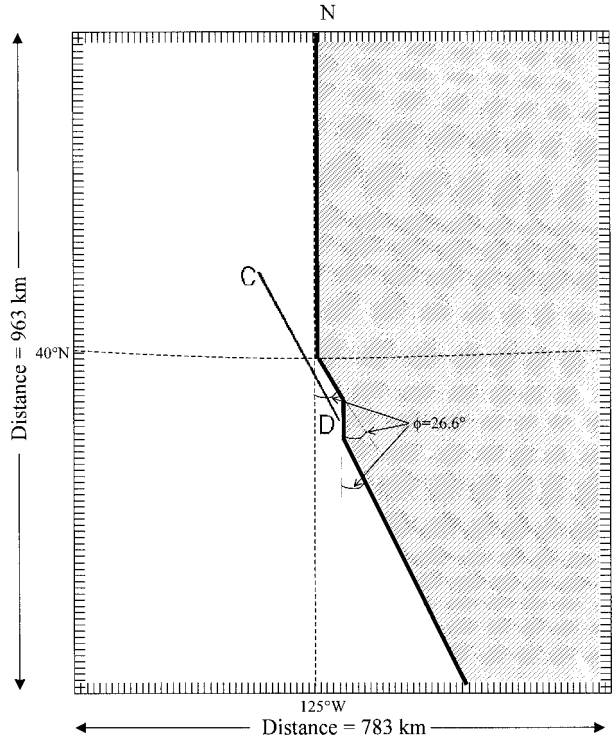

FIG. 11. Full domain and coastline specification for the simulation with three coastal bends. Cross-section plane C–D is also indicated.

second convex bend and the flow remains supercritical, as in the single-bend simulation.

6. Analytical results: Dynamics of vertical trapping

a. Shallow water similarity solutions

In this section we compare the mesoscale numerical model solutions to a shallow water similarity theory for stratified flow due to Yih (1969). Some of the issues raised in this comparison of shallow water theory, which implicitly includes vertical trapping, to the flow of a vertically unbounded, stratified fluid, in which vertical propagation of energy is allowed, are similar to issues that have arisen previously in the theory of mountain waves and severe downslope windstorms (Smith 1985; Durran 1986; Smith and Sun 1987; Durran and Klemp 1987; Durran 1992). Linear wave theory offers some insight into the dynamics but encounters difficulty in connection with the idea of supercritical flow, because wave phase speeds may be arbitrarily large in a vertically unbounded fluid. Nonlinear theories that assume separated lower-level flow beneath a stagnant upper level with uniform pressure yield a shallow water analogy, for which the supercriticality condition is well defined (e.g., Smith 1985). However, such theories do not include effects of rotation, friction, or forcing.

The mountain wave shallow water analogy relies on solutions of Long's (1953) equation for stratified flows that vary only in the vertical and downstream directions, with uniform cross-stream conditions. That analysis cannot be directly adapted to the present case of flow around a bend, because of the intrinsically three-dimensional geometry. However, a family of exact shallow water similarity solutions for stratified, three-dimensional, nonrotating, inviscid, hydrostatic, Boussinesq flow over a flat bed due to Yih (1969) may be used in a similar way in the present case. We refer to these solutions as "shallow water similarity solutions" because they have the property that their horizontal structure is self-similar in the vertical and is given exactly by a solution of an associated set of shallow water equations. That is, the height $Z(x, y, \vartheta)$ of isentropes in the moving layer of thickness $H(x, y)$ is given by $Z = Z_0(\vartheta)H/H_0$, and the horizontal velocities are given by $(u, v) = \Lambda(\vartheta)(U, V)$, where the horizontal structure functions, $H(x, y)$, $U(x, y)$, and $V(x, y)$, are independent of ϑ and satisfy a nondimensional set of shallow water equations. Here $Z_0(\vartheta)$ and H_0 are set by the upstream conditions and

$$\Lambda^2(\vartheta) = gH_0\left\{[\vartheta_H - \vartheta)/\vartheta_H](Z/H) + (\vartheta/H)\int_Z^H (1/\vartheta - 1/\vartheta_H)\, dz\right\},$$

where $\vartheta_H = \vartheta(Z = H)$.

For comparison with the COAMPS results, three-dimensional solutions for supercritical flow around a bend were constructed from these similarity solutions by the following procedure. First, the potential temperature surface $\vartheta = \vartheta_H$ that defines the top $Z = H$ of the moving layer in the similarity solutions is chosen by inspection of the potential temperature and wind speed cross sections. A weakly stratified layer develops downstream of the bend in the numerical solutions (Fig. 3), on ν surfaces near 310–312 K, whose upstream height is 1500–2000 m. Since the upstream wind decreases from 15 m s^{-1} near 500 m to 1–4 m s^{-1} on these surfaces, it appears to be consistent to place the top of the moving layer for the similarity solution in this range of heights. This choice is not entirely objective, as the upstream winds do not quite vanish at any level, reaching a minimum of just under 1 cm s^{-1} at the uppermost level (26 km). Then, $Z_0(\vartheta)$ is defined as a table of the upstream potential temperature values at the grid levels, H_0 is the chosen upstream height of the moving layer, and $\Lambda(\vartheta)$ is evaluated by numerical integration over the grid levels. The upstream wind velocity $U(\vartheta) = U_0\Lambda(\vartheta)$ is determined by the stratification through the profile function $\Lambda(\vartheta)$ up to the constant U_0. The value of U_0 is chosen to match roughly $U(\vartheta)$ to the mesoscale model upstream winds. The shallow water equations are then integrated to obtain $H(x, y)$, $U(x, y)$, and $V(x, y)$, and the corresponding cross sections for ϑ and wind speed

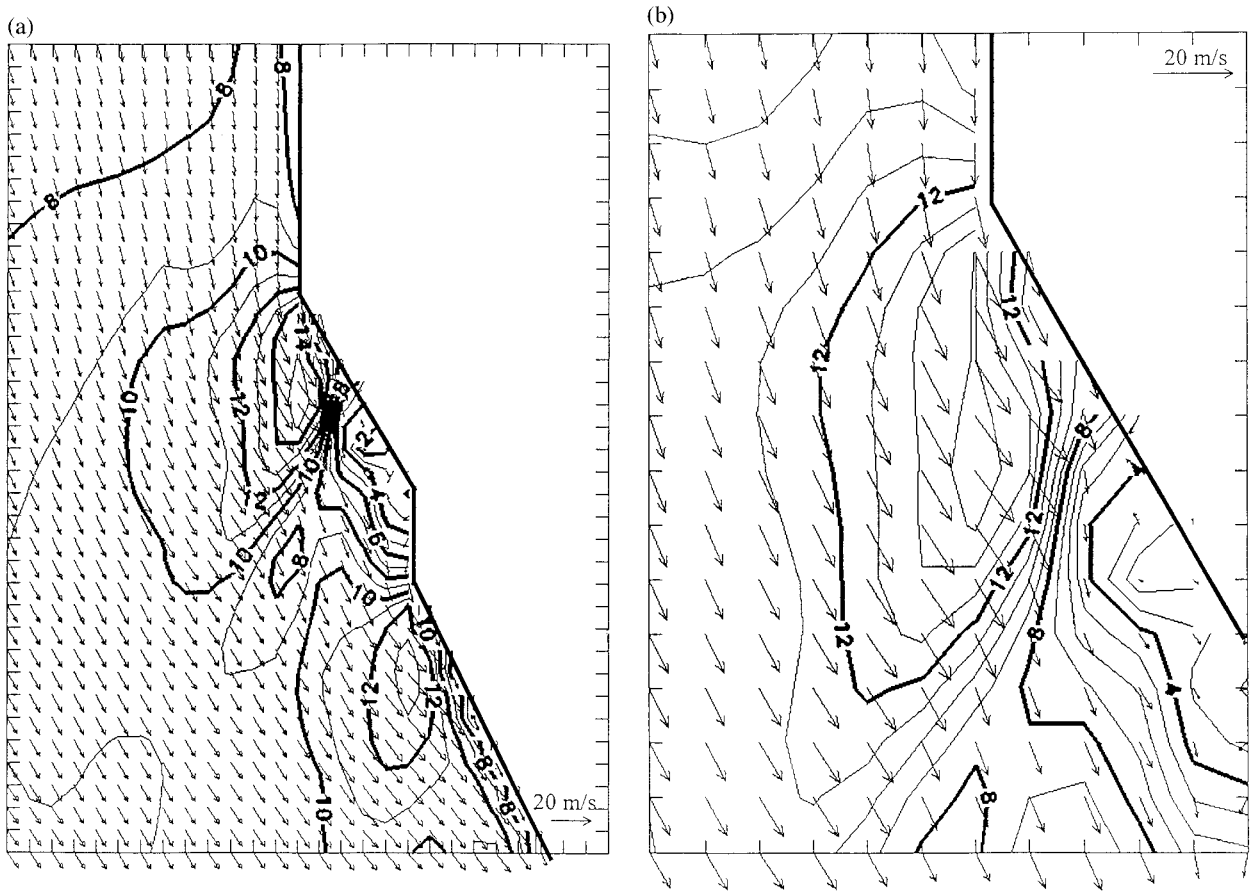

FIG. 12. (a) 10-m wind vectors and isotachs (m s^{-1}) at hour 4 of the multibend simulation, (b) Close-up view of flow field south of first bend where oblique hydraulic jump occurs.

reconstructed from these, using the similarity functions $Z_0(\vartheta)$ and $\Lambda(\vartheta)$.

The resulting cross sections from the similarity solutions chosen to match the benchmark case from the mesoscale model are shown in Figs. 15a,b. These should be compared with Figs. 3a,b. For this similarity solution, the upstream height H_0 of the moving layer was set equal to 1400 m. The decrease in boundary layer thickness and inversion height in the vicinity of the bend is reproduced qualitatively and quantitatively by the similarity solution. The deformation of the isentropes above the inversion is only qualitatively captured by the similarity solution: the 306- and 307-K isentropes merge with the inversion in the mesoscale model but remain above it in the similarity solution, while the 309–311-K isentropes dip too sharply toward the inversion in the similarity solution. The weakly stratified region between 311 and 312 K downstream of the bend in the mesoscale model appears to correspond roughly to the 311-K neutral region between the moving layer and the flat upper isentropes in the similarity solution. In the mesoscale model, this region of weak stratification is not as sharply defined.

The similarity solution reproduces some of the qualitative structure of the velocity field in the mesoscale model (Figs. 15b, 3b), but the correspondence is not as close as for the potential temperature field. Although U_0 has been chosen to match the wind speeds, the structure of the upstream wind profiles do not match closely, as the strongest shear in the similarity solution is near the inversion and near the top of the moving layer, while the strongest shear in the mesoscale model is in the intervening layer between 500 and 1000 m. The similarity solution is inviscid and does not capture the frictional velocity decrease at the base of the surface boundary layer in the mesoscale model. The weak upward slope of the isotachs above the inversion that occurs upstream of the bend in the mesoscale model has no counterpart in the similarity solution, which is uniform upstream of the bend. The similarity solution does qualitatively capture the stronger downward slope of the isotachs above the inversion that occurs downstream of the bend in the mesoscale model, but overestimates the shallowing and vertical compression of these isotachs. The maximum downstream velocity in the similarity solution exceeds 25 m s^{-1}, roughly 5 m s^{-1} greater than the maximum in the mesoscale model, suggesting that friction retards the flow significantly in the mesoscale

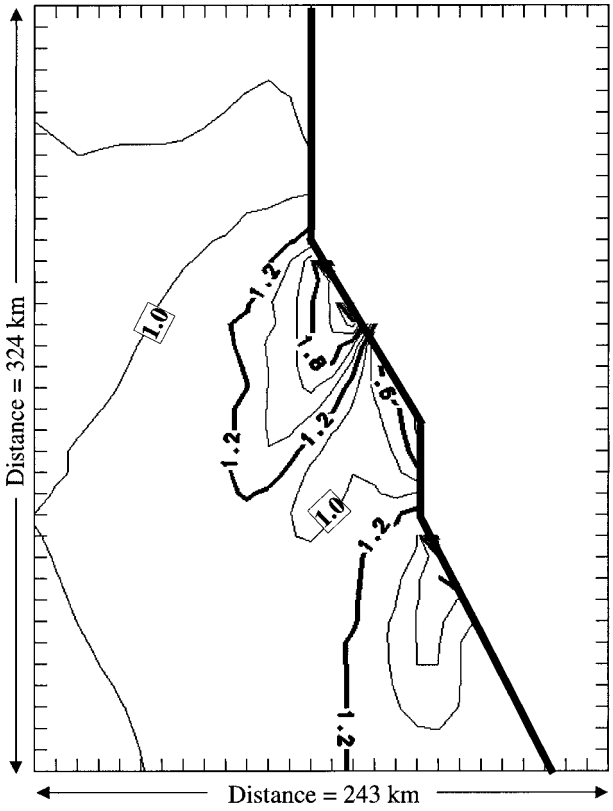

FIG. 13. Froude number computed at hour 4 of the multibend case.

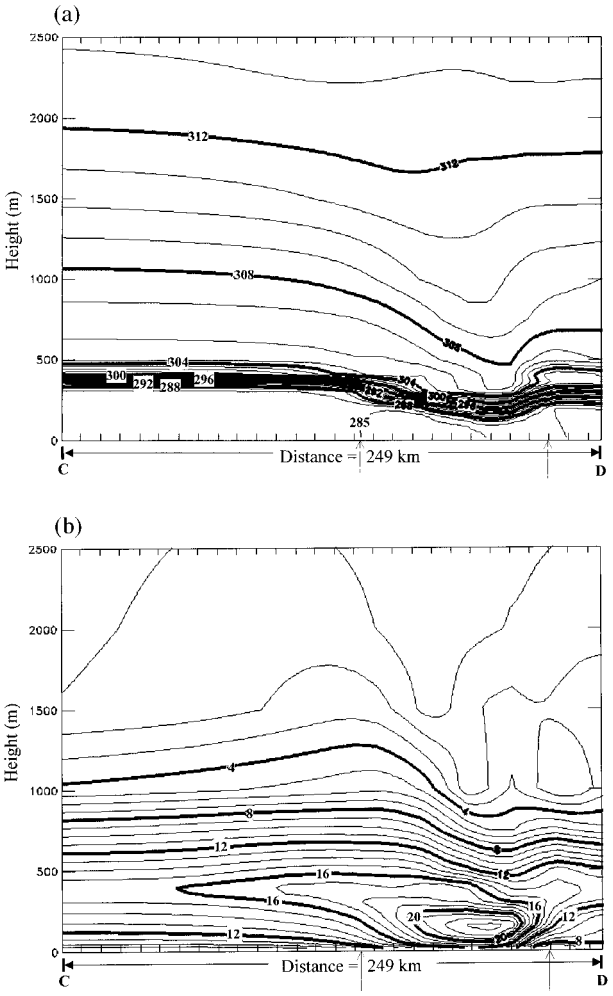

FIG. 14. (a) Potential temperature (K) and (b) wind speed (m s^{-1}) at hour 4 of the multibend simulation. These cross sections are taken along line C–D of Fig. 11. The arrows mark the locations of the first and second bends.

model. The weak upper-level acceleration that extends to altitudes above 3 km near the bend in the mesoscale model is not reproduced by the similarity solution.

The shallow water solution that was used to construct the similarity solution cross sections is shown in Fig. 16. For the benchmark case, the upstream Froude number was one, so the upstream flow is exactly critical. It becomes supercritical when it encounters the coastal bend, as the flow accelerates through the expansion fan and the equivalent height decreases. Downstream of the bend, the Froude number reaches 2.6, with the wind speed increasing by half and the equivalent height falling to one-third of their respective upstream values.

Comparisons of the similarity theory to cases S1 and S2 yielded mixed results. For S2, the similarity form indicated subcritical flow upstream. This is consistent with the Froude number estimate in section 3 but would require a transcritical solution of the shallow water equations for the comparison, which is beyond the scope of the present work. For S1, the similarity form indicates that the upstream flow is still near critical, as the stratification above the inversion does not change. There is slightly less acceleration than in the benchmark case, but the difference is not as dramatic as that in the mesoscale model S1. The near-neutral region above the inversion is not as evident in S1 as in the similarity solution (or the benchmark case). These differences may in part have to do with the relative weakness in S1 of the pressure gradients induced by the disturbance, compared with the large-scale forcing that maintains the shear.

b. Linear theory and vertical trapping

From a more general point of view, it might be assumed that the shallow water model should provide a useful approximation to the dynamics of the simulated flows simply because the stratification is dominated by the sharp rise in potential temperature across the inversion at the top of the well-mixed surface boundary layer. This assumption is implicit in previous modeling of these coastal flows that uses the shallow water model as a direct physical model of the coastal lower atmosphere (Samelson 1992; Samelson and Lentz 1994), rather than in conjunction with a similarity theory. Such an assumption would be supported by linear theory if

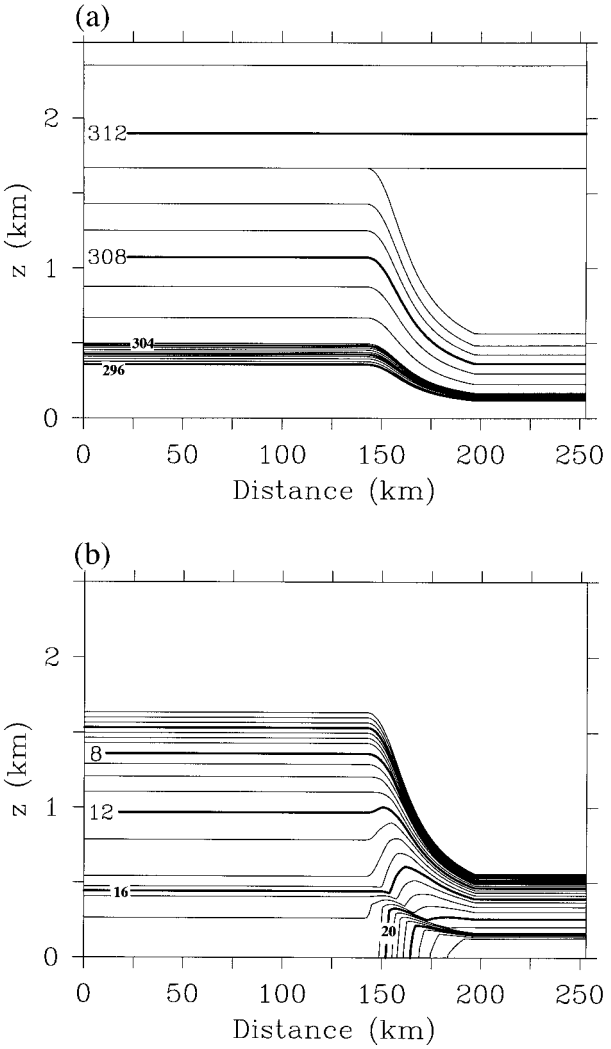

FIG. 15. (a) Potential temperature (K) distribution computed using the Yih (1969) similarity approach for stratified flows. Initialization is based on values from the benchmark mesoscale model case and cross section shown is A–B of Fig. 1; (b) as in (a) except for wind speed (m s^{-1}).

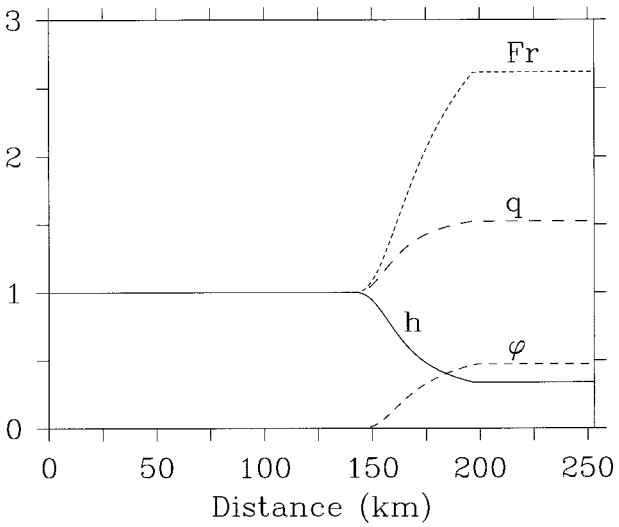

FIG. 16. Shallow water model solution for flow around bend using the initial conditions of the mesoscale model benchmark case. These shallow water results are used in conjunction with the similarity solutions (nondimensional variables: Froude number Fr, wind speed q, MABL depth h, and flow direction φ in radians.)

the linear response to surface forcing were trapped by the stratification associated with the inversion. However, the weak stratification above the inversion is still typically strong enough to support vertical propagation of energy except at very short wavelengths. A stratified fluid with buoyancy frequency N will support vertically propagating plane waves generated at the surface by a horizontal wind U for all horizontal wavenumbers $k < N/U$, which for upper-level $N = 0.01$ s^{-1} and near-surface $U = 10$ m s^{-1} corresponds to wavelengths greater than 6 km. This is several times smaller than the characteristic horizontal scale of the isentrope deformations around the coastal bend, suggesting that trapping due solely to the stratification profile is insufficient. In addition, the isentropes just above the boundary layer are deformed more than the inversion itself, which also is inconsistent with trapping by the stratification.

If vertical propagation is allowed, then the relevant vertical modes (if any exist) would apparently be those for an unbounded stratified fluid. Since these typically have arbitrary phase speed, the flow cannot be supercritical with respect to all of them, and the shallow water analogy becomes problematic. In addition, the vertical decay in the solution with uniform upper-level stratification is inconsistent with a flow structure controlled by the unbounded modes. Orographically trapped modes may also exist, with vertical scale controlled by the 2-km height of the coastal orography in the mesoscale model, but it is not clear why only these special modes would be excited when the flow encounters the coastal bend.

Within the linear theory, ray-tracing and Scorer parameter computations may be used to investigate the trapping effect of the vertical shear of the horizontal wind (e.g., Gill 1982). We briefly summarize the results of such calculations here. Caution must be used in the interpretation of these results, as both rely on the assumption that the mean or upstream flow profiles change slowly with height relative to the vertical scale of the disturbance, which is not strictly satisfied in this case.

Profiles of Scorer parameter

$$l^2(z) = (N/U)^2 - (1/U)\, d^2U/dz^2$$

computed from model profiles along A–B in Fig. 1 tend to be large and positive, indicating vertical propagation everywhere except in a layer near 800–1000 m, where they are small and often negative, indicating a trapped response. These small and negative values are due to the second term in the expression for l^2, the curvature

of the vertical profile of horizontal wind. Since this layer is relatively thin, wave-tunneling through the evanescent zone can be anticipated, rather than complete trapping. However, the ray-tracing calculation also suggests that the vertical shear of the horizontal wind favors low-level confinement of the response to the coastal bend. The linear analysis thus implicates the vertical shear of the horizontal wind in the vertical trapping of the response, but it does not yield quantitative results that are comparable to the shallow water similarity theory.

7. Conclusions and summary

The NRL COAMPS mesoscale model is used to address the wall-bounded flow characteristics of fully stratified flow over a range of initial Froude numbers (Fr). Flow around a single, simple convex bend initially is investigated with Fr varied from subcritical to supercritical by altering the strength of the MABL capping inversion. Strong drops in MABL depth and flow acceleration occur as the flow rounds the bend, in agreement with expectations from simple shallow water models. However, the mesoscale model indicates the presence of strong flow perturbations in the stratified atmosphere above the MABL inversion as well, a feature untreated by standard shallow water approaches. Further, COAMPS indicates that the most intense flow acceleration occurs in a transcritical simulation where the flow upstream of the bend is subcritical but becomes supercritical upon rounding the bend. This is analogous to the situation wherein particularly strong downslope winds often occur, namely, when upwind subcritical flow becomes supercritical as it plunges down a mountain's lee slope. When the wind speed is light and the flow remains subcritical on either side of the bend, the spatial character of the flow perturbation is remarkably different than cases containing supercritical flow. Whereas with supercritical expansion fans the flow adjusts very abruptly downstream of the bend, in fully subcritical flow the perturbations are considerably more diffuse and symmetric about the coastal bend.

We also have explored simulations of flow around multiple bends in the coastline (Fig. 11). An expansion fan forms about each of the two convex bends. However, the middle, concave bend blocks the flow in the expansion fan around the first bend and induces a supercritical to subcritical flow transition. Along this line of transition in Fr from greater to less than 1, a hydraulic jump forms. This jump is evidenced in the mesoscale model results by an abrupt decrease in wind speed, a change in wind direction, an increase in MABL depth, and an increase in surface pressure. This hydraulic jump is detached from the vertex of the concave bend; it appears upstream of this location. Well-known shock–angle relationships (Ippen 1951) confirm that a detached shock is to be expected for the flow conditions in this simulation.

The class of problems addressed here with the mesoscale model is deliberately rather simple so that comparison may be made with idealized shallow water models. Care has been taken to minimize forcing by surface fluxes and other synoptic-scale baroclinic processes, and integration has proceeded until approximate stationarity is obtained. Under these idealized conditions, comparison may be made with a family of solutions (Yih 1969) for stratified flow whose horizontal structure is described exactly by solutions of an associated set of shallow water equations. Despite the absence of rotation, friction, and forcing, these solutions show qualitative agreement with several aspects of the mesoscale model results, including the tendency for strong deformation of isentropes above the inversion, which is not represented in the traditional shallow water theory. The existence of this similarity family suggests that previous shallow water results (Samelson 1992; Samelson and Lentz 1994; Rogerson 1999) might be reinterpreted in a similar manner as approximate solutions for continuously stratified flow. The nonlinear similarity solutions and the linear Scorer parameter and ray-tracing calculations all suggest that the vertical confinement of the disturbance induced by the bend is due more to the vertical shear than to the stratification, though the dynamical relation between the mechanisms in the linear and nonlinear cases is uncertain. We conclude that the existence of a supercritical flow response around coastal bends may depend more on the presence of a low-level jet than on the presence of a sharp boundary layer inversion.

Acknowledgments. The authors thank A. Rogerson for helpful comments and L. B. Nance for bringing to our attention the cited references on downslope windstorms. Discussions with Jim Doyle, Jerry Schmidt, and Rich Hodur proved helpful. Also, the comments of the reviewers were very helpful. This work was supported by the Office of Naval Research, Program Element 0601153N and, for RS, by ONR Grant N00014-93-1-1369, Code 322MM.

REFERENCES

Bridger, A. F. C., W. C. Brick, and P. F. Lester, 1993: The structure of the marine inversion layer off the central California coast: Mesoscale conditions. *Mon. Wea. Rev.,* **121,** 335–351.

Burk, S. D., and W. T. Thompson, 1996: The summertime low-level jet and marine boundary layer structure along the California coast. *Mon. Wea. Rev.,* **124,** 668–686.

Doyle, J. D., 1997: The influence of mesoscale orography on a coastal jet and rainband. *Mon. Wea. Rev.,* **125,** 1465–1488.

Durran, D. R., 1986: Another look at downslope windstorms. Part I: The development of analogs of supercritical flow in an infinitely deep, continuously stratified fluid. *J. Atmos. Sci.,* **43,** 2527–2543.

——, 1992: Two-layer solutions to Long's equation for vertically propagating mountain waves: How good is linear theory? *Quart. J. Roy. Meteor. Soc.,* **118,** 415–433.

——, and J. Klemp, 1987: Another look at downslope windstorms. Part II: Nonlinear amplification beneath wave-overturning layers. *J. Atmos. Sci.,* **44,** 3402–3412.

Elliott, D. L., and J. J. O'Brien, 1977: Observational studies of the

marine boundary layer over an upwelling region. *Mon. Wea. Rev.*, **105,** 748–761.
Enfield, D. B., 1981: Thermally driven wind variability in the planetary boundary layer above Lima, Peru. *J. Geophys. Res.*, **86,** 2005–2016.
Enriquez, A. G., and C. A. Friehe, 1995: Effects of wind stress and wind stress curl variability on coastal upwelling. *J. Phys. Oceanogr.*, **25,** 1651–1671.
Freeman, J. C., 1950: The wind field of the equatorial east Pacific as a Prandtl-Meyer expansion. *Bull. Amer. Meteor. Soc.*, **31,** 303–304.
Gill, A. E., 1982: *Atmosphere–Ocean Dynamics.* Academic Press, 662 pp.
Hodur, R. M., 1997: The Naval Research Laboratory's Coupled Ocean/Atmosphere Mesoscale Prediction System (COAMPS). *Mon. Wea. Rev.*, **125,** 1414–1430.
Ippen, A. T., 1951: Mechanics of supercritical flow. *Trans. Amer. Soc. Civil Eng.*, **116,** 268–295.
Long, R. R., 1953: Some aspects of the flow of stratified fluids I. A theoretical investigation. *Tellus,* **5,** 42–58.
Rogers, D. P., and Coauthors, 1998: Highlights of coastal waves 1996. *Bull. Amer. Meteor. Soc.*, **79,** 1307–1326.
Rogerson, A. M., 1999: Transcritical flows in the coastal marine atmospheric boundary layer. *J. Atmos. Sci.*, **56,** 2761–2779.
Samelson, R. M., 1992: Supercritical marine-layer flow along a smoothly varying coastline. *J. Atmos. Sci.*, **49,** 1571–1584.
——, and S. J. Lentz, 1994: The horizontal momentum balance in the marine atmospheric boundary layer during CODE-2. *J. Atmos. Sci.*, **51,** 3745–3757.
Smith, R. B., 1985: On severe downslope winds. *J. Atmos. Sci.*, **42,** 2597–2603.
——, and J. Sun, 1987: Generalized hydraulic solutions pertaining to severe downslope winds. *J. Atmos. Sci.*, **44,** 2934–2939.
Stull, R. B., 1988: *An Introduction to Boundary Layer Meteorology.* Kluwer Academic, 666 pp.
Thompson, W. T., T. Haack, J. D. Doyle, and S. D. Burk, 1997: A nonhydrostatic mesoscale simulation of the 10–11 June 1994 coastally trapped wind reversal. *Mon. Wea. Rev.*, **125,** 3211–3230.
Winant, C. D., C. E. Dorman, C. A. Friehe, and R. C. Beardsley, 1988: The marine layer off northern California: An example of supercritical channel flow. *J. Atmos. Sci.*, **45,** 3588–3605.
Yih, C.-S., 1969: A class of solutions for steady stratified flows. *J. Fluid Mech.*, **36,** 75–85.